JOURNAL OF SOLID STATE CHEMISTRY 45, 259–275 (1982)

Structures of Hexagonal Vanadium Fluoride Bronzes: A High-Resolution Electron Microscopic Study

DAVID RIECK, R. LANGLEY,* AND L. EYRING†

Department of Chemistry and the Center for Solid State Science, Arizona State University, Tempe, Arizona 85287

Received February 15, 1982; in revised form June 25, 1982

At least three and possibly four phases are shown to exist in the system A_xVF_3, where A = K, Rb, Cs, and Tl and x = 0.19–0.32. The α_I phase has the hexagonal tungsten bronze structure with a doubled c axis. For this structure there is one hexagonal tunnel containing two A sites per unit cell. Calculated electron microscope images, assuming that only one layer of A atom sites is occupied, simulate experimental images of this phase from both the [001] and [100] directions. The α_{II} phase is an orthorhombic superstructure containing two tunnels and four A sites per unit cell. Comparison of observed and calculated images shows one tunnel to be more fully occupied than the other. The α_{IV} phase has a c axis the length of six octahedra. Its existence is shown by diffraction patterns and fringe images. The existence of an α_{III} phase, having four hexagonal tunnels per unit cell, is suggested on the basis of diffraction patterns.

Introduction

In a recent paper, Hong *et al.* (*1*) reported studies of a series of compounds with the general formula A_xVF_3 with A = K, Rb, Cs, or Tl and x ranging from 0.19 to 0.32. These compounds were first synthesized by Cros *et al.* (*2*), who reported them to have structures derived from the Magnéli hexagonal tungsten bronze (HTB) structure (*3*). The axis lengths for $K_{0.25}VF_3$ are a = 7.41 and c = 7.51 Å (*2*). Figure 1 illustrates this structure, where VF_6 octahedra share corners to produce a hexagonal array of large (≃5 Å diameter) tunnels parallel to the c axis and occupied by the A cations. The distortions from hexagonal symmetry discussed by Hong *et al.* (*1*) are too small to be significant in electron microscopy. For the purposes of this paper, the samples will be referred to as simply hexagonal, rather than pseudohexagonal. All the superstructures described here have the hexagonal K_xWO_3 substructure with a c axis twice the length of a coordination octahedron, hence two A atom positions per unit cell. The further ordering discussed here results from variations of the occupancy of the tunnels.

Cros *et al.* reported the product of their synthesis of the hexagonal compounds to be a single phase, and designated it α. An electron diffraction study (*4*) of the samples synthesized by Boo revealed the presence of a hexagonal phase and two related orthorhombic phases, which result from the doubling of one or two of the a axes of the HTB structure. These phases are here labeled α_I, α_{II}, and α_{III}, while in Ref. (*4*) they were

* Present address: Department of Chemistry, Stephen F. Austin State University, Nacogdoches, Texas 75961.

† Author to whom inquiries should be made.

0022-4596/82/140259-17$02.00/0

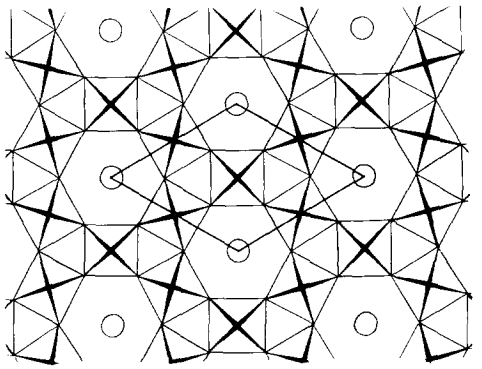

FIG. 1. An idealized model of the hexagonal tungsten bronze structure projected down the c axis, with the unit cell outlined.

referred to by their respective Roman numerals only.

Phase α_{II} results from the doubling of one a axis, while α_{III} results from doubling two of the a axes. This doubling was ascribed (*1, 4*) to a possible ordering of the alkali metal or thallium ions. Here high-resolution electron microscopy is used to clarify the nature of this ordering both among and within the tunnels and an additional phase is introduced. In addition, the compositional relationships between structures at different temperatures are considered qualitatively.

Experimental

During the course of this investigation samples of 14 different compositions, supplied by W. O. J. Boo,[1] were examined. These compositions (for A_xVF_3) were for A = K, Rb, $x = 0.225$; A = K, Rb, Cs, or Tl, x = 0.18 and 0.25; A = K, $x = 0.27$; A = Cs, x = 0.31; A = Rb, $x = 0.32$; and A = Tl, x = 0.30. The samples were ground under liquid nitrogen, suspended in acetone, and mounted on holey carbon films supported on copper microscope grids. Electron diffraction patterns and lattice images were obtained on a JEM 100B transmission electron microscope operated at 100 kV according to procedures described by Iijima (*5, 6*). Images and diffraction patterns in the mutually perpendicular [001], [100], and [120] zones were obtained and compared with calculated images.

Image calculations were carried out on a model for the A_xVF_3 structure derived from that of HTB by assuming ideal geometry. The A atoms were placed at $z = 0$ and $\frac{1}{2}$, at the centers of the hexagonal tunnels in the 18 coordinate sites. It was assumed that the VF_3 sublattice was composed of perfect VF_6 octahedra sharing all corners to produce a hexagonal array, and that these octahedra were lined up parallel to c so that all layers of octahedra were identical. The c axis of this structure is one-half of the length of that observed. This indicates that the c axis is doubled by some distortion of the VF_3 substructure from the ideal geometry used in the calculated images. For the calculated images only the occupancies of the A sites were varied. The similarity between the observed and calculated images indicates that this approximation is adequate.

Images were calculated by the n-beam multislice method originated by Cowley and Moodie (*7*). The computer package used was written by Skarnulis *et al.* (*8*) with extensive modifications by O'Keefe *et al.* (*9*). The programs used were FOCO 3200, DEFRACT 1500, and IMAGE 1500. Image calculation parameters are given in Table I. Errors in thickness and defocus are estimated to be about ±1 slice and ±25 Å, respectively. The image program includes contributions from partial beams and so allows the objective aperture size to be used to vary the resolution continuously over a small range to give the most correct aperture function.

Calculations and computer graphics for

[1] W. O. J. Boo, Department of Chemistry, University of Mississippi, University, Mississippi 38677.

Figs. 2 and 7 were done on our recently developed user interactive image calculation system (*10*). The average experimental unit cell is calculated by digitizing an area of a microscope plate on an automicrodensitometer, defining a unit cell on the digitized image, and calculating the arithmetic intensity average of all unit cells in the chosen area, point by point. The correlation coefficients associated with Fig. 7 are calculated by normalizing the simple arithmetic difference between the intensity of each point in an averaged unit cell and the corresponding point in a calculated unit cell. A correlation coefficient of unity corresponds to exact equivalence. An adjustment is made for differences in the overall intensity of the images compared.

Quantitative elemental analyses were carried out using a Princeton Gamma-Tech energy-dispersive X-ray analysis system on a JEOL JSM-35 scanning electron microscope operated at 15 kV. A standard ZAF correction was applied to the raw signal. Analyzed crystals were mapped on photographs, and their diffraction patterns were

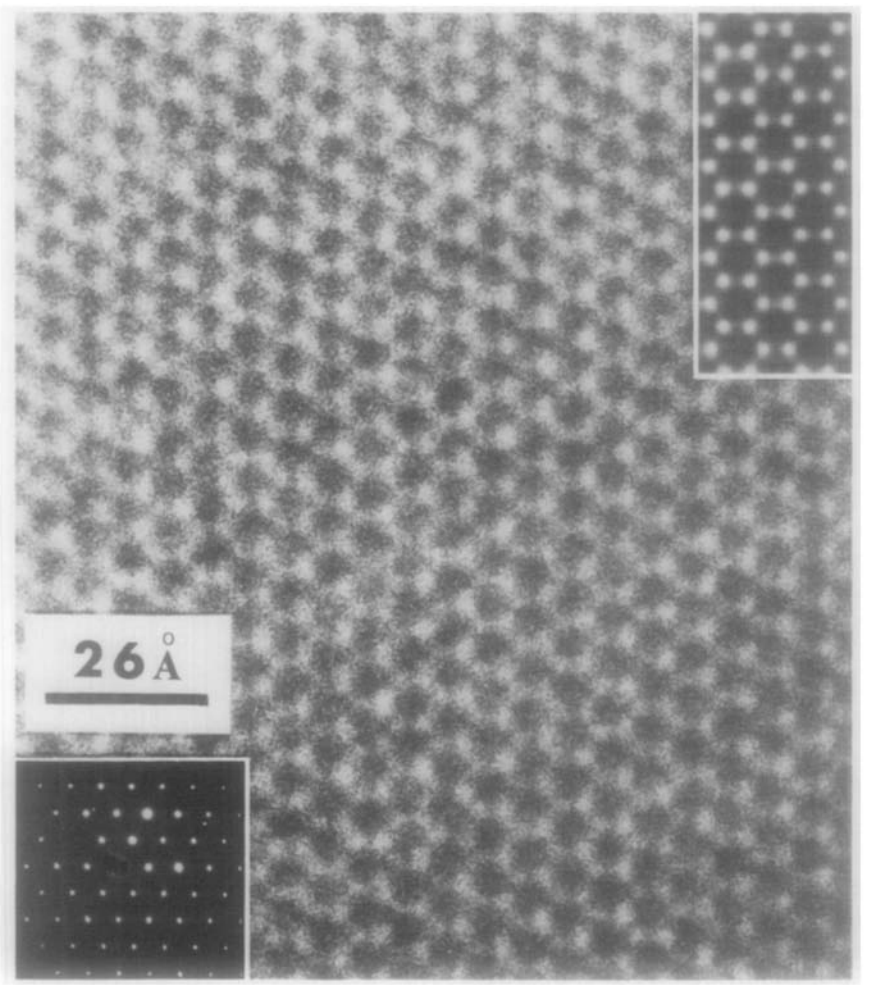

FIG. 2. An image of phase α_1 of $K_{0.25}VF_3$ projected down *c*. The inset at the upper right shows the calculated image while the one at the lower left shows the diffraction pattern.

TABLE I

IMAGE CALCULATION PARAMETERS

Figure	Zone	Sample	Number of slices	Thickness (Å)	Defocus (Å)	Objective aperture radius ($Å^{-1}$)
2	[001]	$K_{0.25}VF_3$	10	75.30	−875	0.28
3	[001]	$K_{0.25}VF_3$	20	150.60	−800	0.27
4	[100]	$K_{0.25}VF_3$	3	22.38	−900	0.285
4	[100]	$K_{0.25}VF_3$	6	44.76	−900	0.285
5	[001]	$Rb_{0.18}VF_3$	8	60.24	−1100	0.28
6	[001]	$Rb_{0.18}VF_3$	8	60.24	−1100	0.26
7	[120]	$K_{0.27}VF_3$	5	64.40	−900	0.27

Note. A spherical aberration coefficient of 1.8 mm, a convergence semiangle of 1.2 mrad, and chromatic half-width of 120 Å were used in all calculations reported. The zone indices are for the hexagonal subcell.

taken on a JEM 100B transmission electron microscope.

Results

Several different superstructures were observed in the samples. Three of them can be differentiated by their *c* axis diffraction patterns, and are associated with phases α_I, α_{II}, and α_{III}. The [001] diffraction pattern of α_I is hexagonal, while the diffraction pattern of α_{II} has superlattice spots halfway between each spot along all rows in a single [100] direction. The unit cell of phase α_{III} is doubled along the equivalent axes [100] and [010]. A summary of the occurrence of these phases at each composition is given in Table II. Entries for α_{IV} are obtained from [100] diffraction patterns. Other data for Table II are based on the *c* axis diffraction patterns of from five to ten crystals of each sample, except for the samples $Rb_{0.18}VF_3$, $Rb_{0.25}VF_3$, $K_{0.225}VF_3$, and $K_{0.25}VF_3$, which were studied much more extensively while investigating phase α_{IV}, and various defects.

Only the most general statements about the occurrence of these phases can be made. An explanation of the occurrence of the different structures will be proposed in the discussion. It is seen that α_{II} is more common than the other phases except in the cesium samples, where α_I occurs more often. There is a tendency for samples with larger x values to form α_I, especially in cesium-containing specimens. At $x = 0.33$ all of the *A* sites would be occupied and doubling of an *a* axis by ordering of the *A* atoms would be unlikely without other structural changes. The α_I phase is defined in this context only as having two equivalent *a* axes, since this is all the information obtainable from diffraction in the [001] direction.

The α_{IV} phase is evidenced by the existence of superlattice spots tripling the *c* axis on [100] diffraction patterns. This phase is present only in trace amounts in samples of $Rb_{0.225}VF_3$, $K_{0.225}VF_3$, and $Rb_{0.25}VF_3$.

It becomes apparent, particularly in

TABLE II

PHASE COMPOSITION OF MICROSCOPE SPECIMENS

Phase observed	Nominal A_x values in A_xVF_3
α_I only	$Cs_{0.25}$, $Cs_{0.31}$
$\alpha_I + \alpha_{II}$	$K_{0.225}$, $K_{0.25}$, $K_{0.27}$, $Tl_{0.25}$, $Cs_{0.19}$
Mostly α_{II}	$K_{0.15}$, $Rb_{0.18}$, $Rb_{0.25}$, $Rb_{0.32}$, $Tl_{0.166}$, $Tl_{0.30}$
Contains α_{III}	$K_{0.18}$, $Rb_{0.18}$, $Tl_{0.166}$, $Tl_{0.30}$
Contains α_{IV}	$Rb_{0.225}$, $Rb_{0.25}$, $K_{0.225}$

studying α_{II}, that the ordered alternate tunnels were not simply either occupied or vacant. Such ordering does not account well for the occurrence of α_{II} in compositions in which it is found, nor did a model of this type produce a calculated image which matched the observed image well. For these reasons calculations using fractional occupancy factors for the *A* cations were tried. Within the limitations described in the cases given, this technique appears to be of value in determining the occupancy of the tunnels by *A* atoms. It was particularly useful in characterizing the α_{II} phase. We are not aware that calculated images have previously been used to estimate fractional occupancy factors in tunnel structures.

Structure of the α_I Phase

The electron diffraction pattern of α_I is not orthorhombic as is the Guinier X-ray diffraction pattern of the bulk sample (*1*); rather it is a simple hexagonal array of spots. However, the presence of crystals with superstructure would, for powder diffraction, mask the existence of those without superstructure. Assuming that this phase is nearly isostructural with the HTB structure, there are two *A* sites per unit cell, at $z = 0$ and $\frac{1}{2}$, within the hexagonal tunnels. Structure images down the *c* axis consist of dark spots in a hexagonal array with six light spots surrounding them. The contrast is inverted at low defocus values. Figure 2 shows an image of the former type from a sample with the composition $K_{0.25}VF_3$, with the diffraction pattern and a calculated image included as insets. Since it was considered possible that the sample contained two phases with greatly differing compositions, calculations were made on models with a wide range of *A* atom occupancy factors.

It is assumed in the model for the calculated image (inset, Fig. 4) that all of the potassium sites at $z = 0$ are filled and all of the sites at $z = \frac{1}{2}$ are empty. This gives an overall sample composition of $K_{0.17}VF_3$. This composition also corresponds to a uniform overall occupancy of 0.5 in the direction of the beam. The match of the calculated with the observed image illustrated in Fig. 2 appears to be satisfactory. The light spots surrounding the dark tunnel, while appearing to correspond to the unoccupied trigonal tunnels apparent in Fig. 1, are well below the resolution of the microscope.

A comparison of an averaged experimental image with images calculated assuming different potassium occupancy factors is shown in Fig. 3. The dark spots in the averaged image and in the occupancy = 0.5 image represent the hexagonal tunnels. The white background should be viewed as interlocking rings around each tunnel. The averaging process has made the small white center dots, apparent in the occupancy = 0.5 image, less distinct than in the calculated image or in some experimental images. The averaging has also overemphasized a trigonal symmetry not obvious in the raw experimental image, Fig. 2. This trigonal symmetry is possibly due to a slight shift of the potassium ions away from the center of the site.

In the calculated images, the central white dots increase in intensity dramatically relative to the white rings as the potassium occupancy increases. At an occupancy of 0.5, the white dots are just visible. They increase in intensity until at 1.0 they are the main feature and the rings have nearly disappeared. This contrast reversal takes place with a change of only 6% in the unit cell weight. Under favorable circumstances, an estimate of the occupancy factor based on image comparison should have an error less than ± 0.1. Changing thickness or defocus can affect the image in much the same way that changing the occupancy factor does. Uncertainties in these and other imaging parameters limit the accuracy of the estimates of occupancy factors made in this paper to about ± 0.2 or ± 0.3.

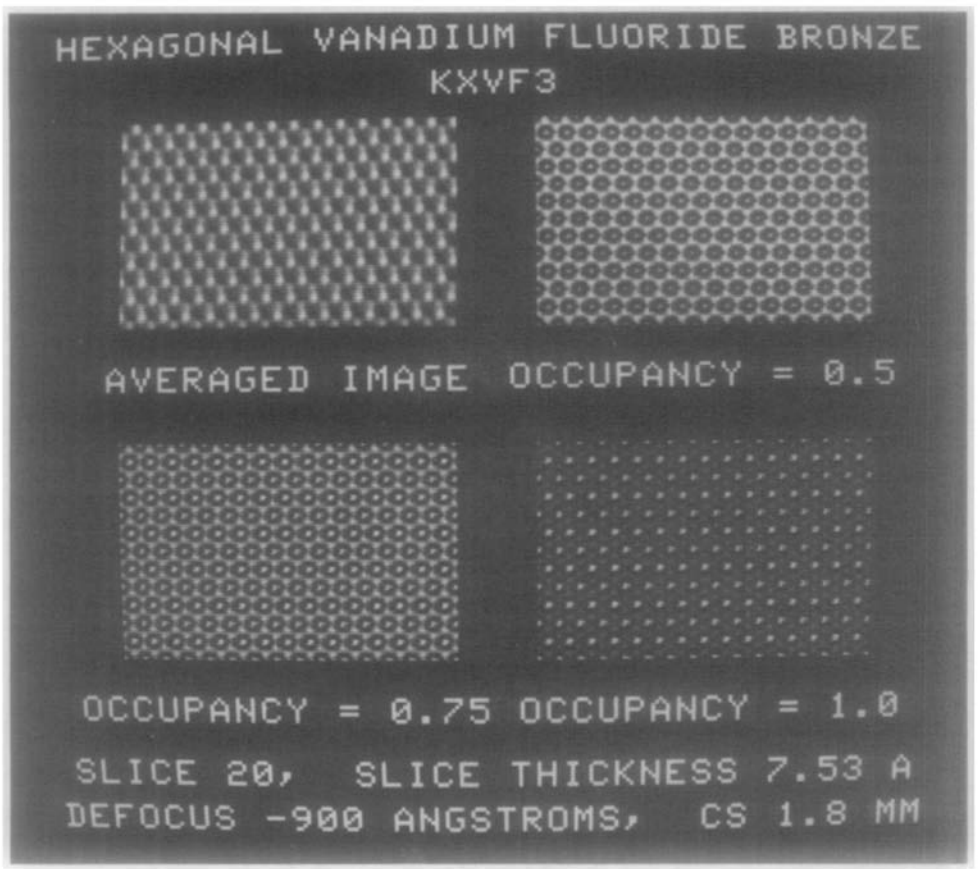

FIG. 3. Comparisons between an averaged experimental image and images calculated with different potassium occupancy factors.

Since neither microscopic observation nor the multislice method of calculation detects differences in models of ordering in the direction of the beam, it is necessary to image crystals from another direction to investigate possible ordering along the c axis. Figure 4 shows a thin edge of a crystal of $K_{0.25}VF_3$ along [100] with images calculated at two thicknesses (22.47 and 44.94 Å) inset for comparison. The crystal gains in thickness toward the top.

The model used in this calculation, identical with that used to calculate the image in Fig. 2, has alternating filled and empty potassium sites. The occupied layer yields a streak in the thin image, becoming a modulated streak in the thicker image. The large white dots correspond to the projection of a row of empty potassium sites. This image match demonstrates that a regular ordering along the c axis exists, however, occupancy factors are still only approximate.

The image of the thick part of this crystal was similar to the thick crystal [100] images of α_1 for all A cations. The detail is lost from the image for thicknesses much above 100 Å, leaving only one spot per unit cell. It is therefore uncertain whether a given [100] image is of a structure having the two A sites equivalent, or if the crystal is just too thick to allow them both to be resolved. No regions less than 100 Å thick were imaged for Rb, Cs, or Tl specimens, and so the evidence for ordering along the c axis for

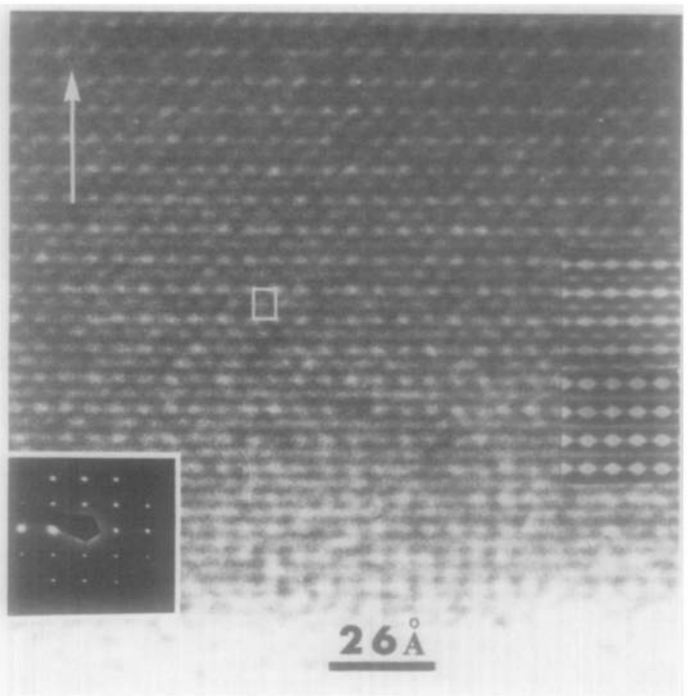

FIG. 4. An image of phase α_I of $K_{0.25}VF_3$ projected down *a*. The horizontal direction is parallel to [120], and *c* is marked by an arrow. The calculated images are for thicknesses of 27.47 (lower) and 44.94 Å (upper). The diffraction pattern is also inset, and a projection of the unit cell is outlined.

these *A* atoms is less certain. Since the *c* axis is approximately the same length for all *A* atoms, a similar ordering may be expected.

Structure of the α_{II} Phase

Lattice images confirm the earlier conclusion based on electron diffraction studies that α_{II} is a superstructure of α_I. The orthorhombic α_{II} unit cell is derived from that of α_I in the following way. Refer to the diagram in Fig. 5. Each dot represents a hexagonal tunnel, all of which are equivalent for α_I. Choosing a tunnel as the origin, the unit cell is defined by an *a* vector linking tunnels to form a row of identical tunnels, a *b* vector linking alternate rows of tunnels, and a *c* vector parallel to the tunnels. The unit cell dimensions, revised since (*4*), are approximately $a = 7.39$, $b = 12.88$, and $c = 7.53$ Å (*1*). The [010] direction of phase α_{II} is therefore the [120] direction of the hexagonal subcell. For convenience all of the indices in this paper refer to the hexagonal

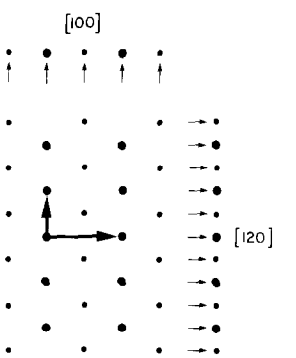

FIG. 5. A diagram of the relationship between α_I and α_{II}. The different-sized dots represent hexagonal tunnels with different *A* atom occupancy factors. The rows of dots on the side and top show the projected repeat distances in the indicated (hexagonal index) directions.

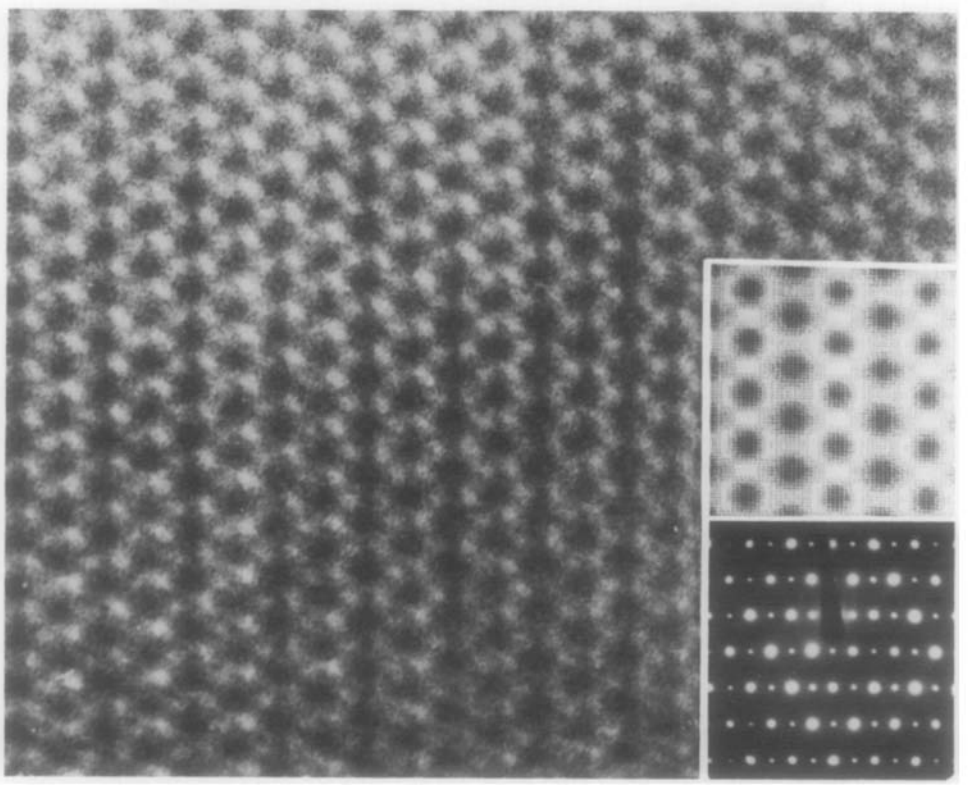

FIG. 6. An image of phase α_{II} (for $Rb_{0.18}VF_3$) with an inset showing the calculated image for $Rb_{0.15}VF_3$) and the [001] diffraction pattern.

subcell. The *a* and *c* axes are the same in phase α_I as in α_{II}. Projections of rows of tunnels down the *a* axis are separated by 6.5 Å. Projection down [120] shows repeat distances of 3.70 Å for α_I and 7.39 Å for α_{II}.

In α_{II}, rows of tunnels alternate in their contrast in accord with the doubling of one of the *a* axes indicated by the superlattice spots in the [001] electron diffraction pattern. In Figs. 6 and 7, a comparison is shown between lattice images from $Rb_{0.18}VF_3$ and two calculated images. The calculated image in Fig. 6 was obtained from a model having Rb occupancy factors of 0.4 and 0.5, respectively, for the tunnels surrounded by six light spots and the dark tunnels between. This gives an overall composition of $Rb_{0.15}VF_3$. For Fig. 7 the light-ringed tunnels have an occupancy factor of 0.5 and the dark tunnels 0.75, giving an overall composition of $Rb_{0.21}VF_3$. The white spots in the dark tunnels (marked by the arrow) appear in calculated images for occupancy factors of about 0.60 or greater.

Image calculations of α_{II} with compositions intermediate between the two models do not appear to improve the match with the observed images. For example, agreement with the size of the white centered dots can be achieved at the expense of the match with the ring of lighter spots. The occupancy ratio of the two rows is as important as the absolute values of the occupancies themselves. All reasonably successful models have about the same ratio, although the composition range covered was large. Images calculated using models where one tunnel was fully occupied gave

an unsatisfactory match.

Images at greater thicknesses or different defocus where there was no hint of the six halo spots around each tunnel were more closely duplicated by calculations, but these less detailed images were even less sensitive to variations in the occupancy factors. It is imperative in these comparisons to have images of thin regions. A nearly perfect match to two rows of large white spots could be obtained with almost any proposed structure, so that such a comparison was not informative in the case of thick crystals.

Images of phase α_{II} were also obtained from the [120] ([010] orthorhombic) direction. Figure 8 shows such an image from the $K_{0.27}VF_3$ sample. The horizontal separation between the white dots in Fig. 8 is about 7.4 Å. Reference to Fig. 5 shows that this is expected only for the [120] direction, and only in α_{II}. The ratio of the tunnel occupancy factors used in this calculation is close to that used for the [001] phase α_{II} calculations for the rubidium sample, but the overall occupancy in this calculation is higher. The tunnel occupancy factors are 0.68 and 0.95. For this calculation, however, all four *A* atom positions must be described separately, since they do not eclipse each other in this direction. The occupancy factor is 0.4 at (0 0 0), and is 0.95 at the other three positions. The light streaks in the images are at $c = \frac{1}{2}$, and the large

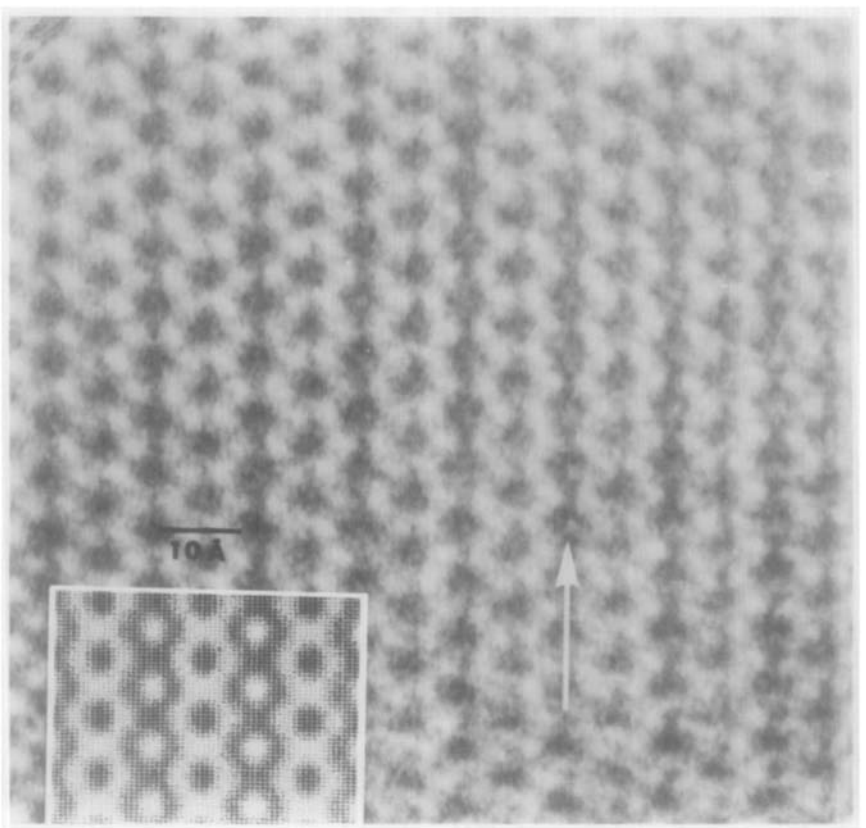

FIG. 7. An image of $Rb_{0.18}VF_3$ (phase α_{II}) projected down [001]. The calculated image inset is for $Rb_{0.21}VF_3$. The arrow marks the row of tunnels assumed in the model to be more completely filled. (Note the white dots at the centers.)

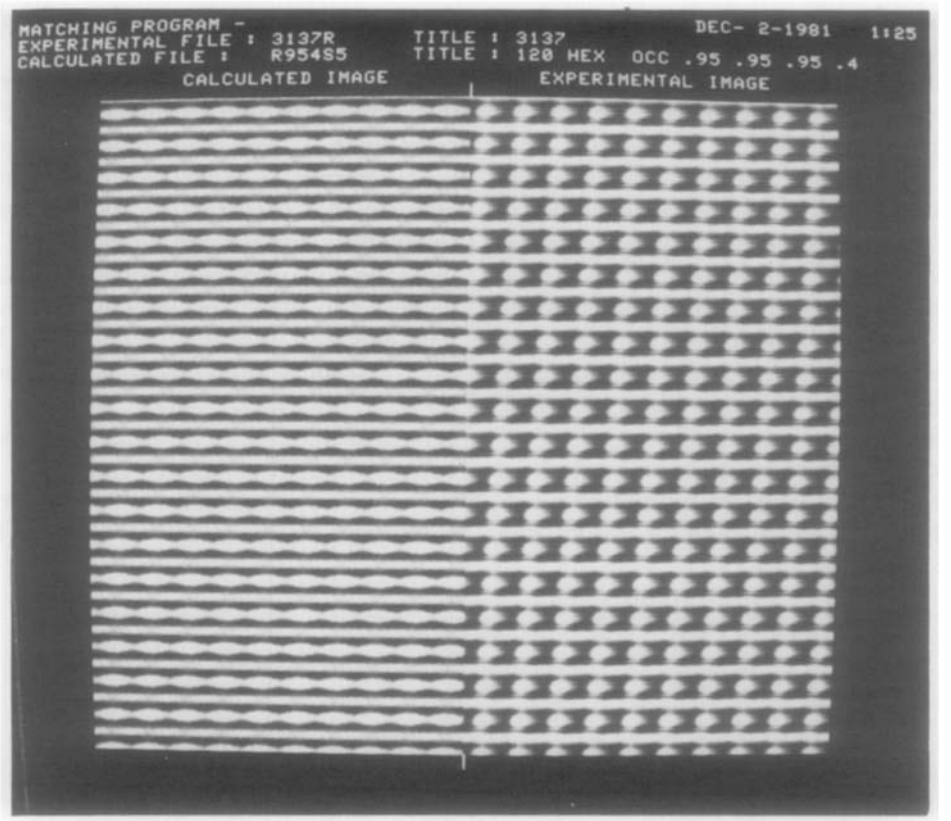

FIG. 8. Phase α_{II} in $K_{0.27}VF_3$ projected down [120]. The c axis is vertical and shows the 3.76-Å spacings. The horizontal direction is the a axis with 7.39-Å repeat spacings. The left side is the calculated image, and the right side is the averaged experimental image.

white dots in the dark streaks are projections through (0 0 0). This image match demonstrates that α_{II} is ordered in the [001] direction as well as in [120].

The agreement between a model and an observed image can be measured by a "correlation coefficient" as described by Rae Smith and Eyring (*10*). The correlation coefficient (CC) for the match in Fig. 8 was 0.747. This compares with 0.687 for a model having three sites fully occupied and one empty, and other similar numbers for the wide range of other models tested. The correlation coefficient provides an objective measure of the correctness of an image match and a quantitative method of comparing different models. Since experimental conditions affect an image in ways that are difficult to account for completely it is not necessarily proven that the model having the highest CC is the best model. This is especially true for CC values less than 0.8. A CC value above 0.85 is a very good match, and the eye cannot readily see any difference between images that correlate above 0.9 (*10*).

Agreement between calculated and observed images from the [120] direction demonstrates that phase α_{II} in the potassium compounds is a superstructure of phase α_I caused by an ordering of the potassium ions. These results are consistent with [001] calculations for the $Rb_{0.18}VF_3$ sample. Within the limitations described above, the

A site at (0 0 0) is less than half occupied, and the sites at ($\frac{1}{2}$ $\frac{1}{2}$ 0), ($\frac{1}{2}$ $\frac{1}{2}$ $\frac{1}{2}$), and (0 0 $\frac{1}{2}$) are nearly fully occupied. The site at (0 0 $\frac{1}{2}$) may have a different occupancy than that of the ($\frac{1}{2}$ $\frac{1}{2}$ 0) or ($\frac{1}{2}$ $\frac{1}{2}$ $\frac{1}{2}$) sites.

Evidence for Other Phases

Diffraction patterns for a few crystals down the *c* axis indicated doubling along two hexagonal *a* directions as shown in Fig. 9. This would result from ordering along two *a* axes to form an orthorhombic cell twice the volume of the α_{II} unit cell (assuming the *c* axis length did not change). This cell is designated α_{III}. Phase α_{III} may be a low-temperature structure which disorders to α_{II} on beam heating. This transition was possibly seen in the microscope, but it always happened too fast for the original α_{III} diffraction pattern to be photographed. Some α_{III} diffraction patterns were stable indefinitely. Unfortunately, images of α_{III} could not be distinguished from those of α_{II}.

Diffraction patterns having superstructure spots on two and sometimes on all three a^* axes also result from twins and from overlays of phase α_{II} rotated by 60° from each other (*11*). These features are easily seen on an image, and areas designated α_{III} do not contain them. There are seldom equal amounts of the different orientations in the diffraction aperture, so the resulting sets of superstructure spots are not of equal intensity. For twins, the intensity is also shifted away from the central spot in a different direction for each set of superstructure spots, according to the location of the domains in the aperture. There is no evidence for twinning on a unit cell level as another possible cause of the α_{III} diffraction pattern.

A few examples of a tripled *c* axis were

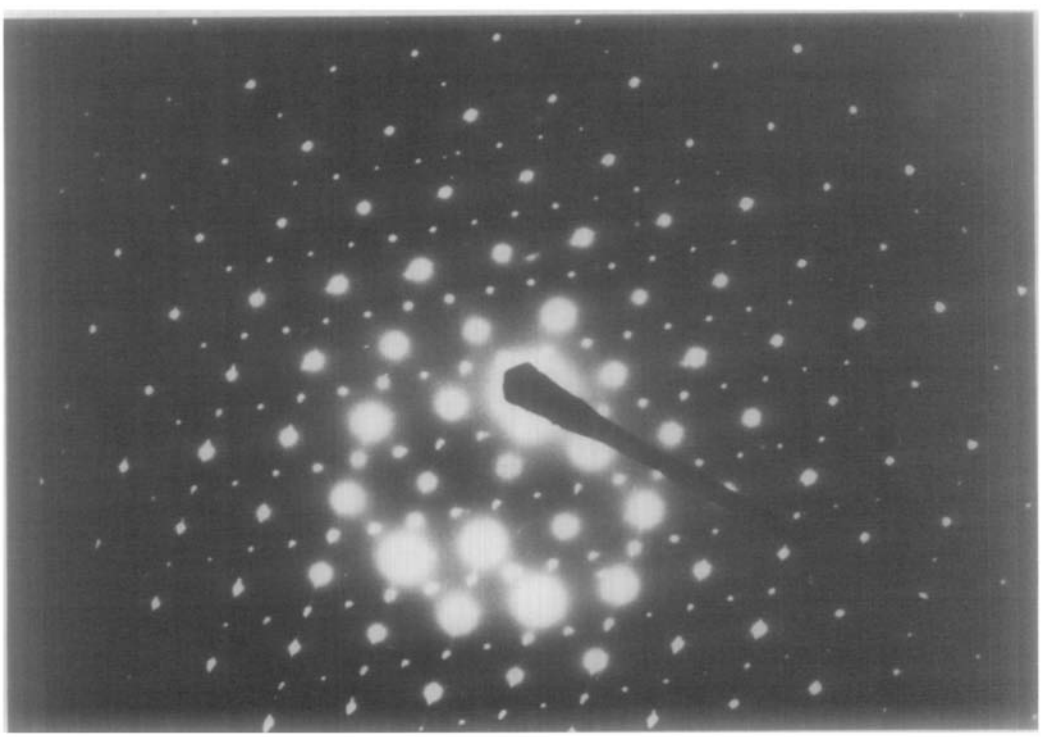

FIG. 9. An electron diffraction pattern for phase α_{III} showing equal intensities of the superstructure spots.

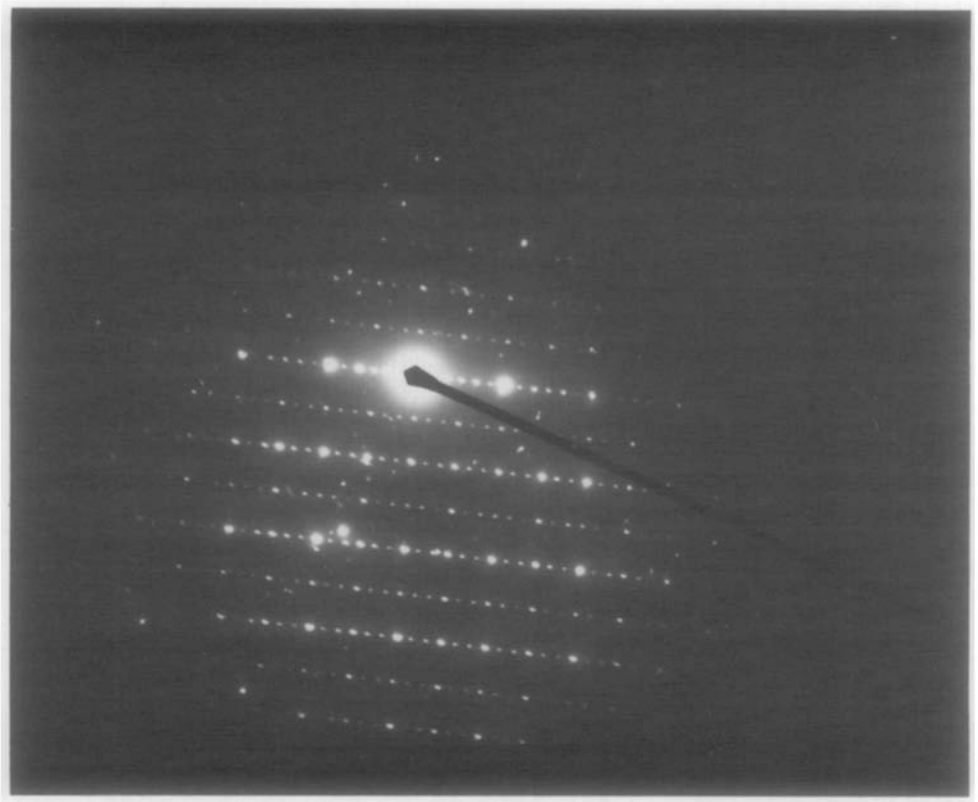

FIG. 10. A diffraction pattern of $Rb_{0.225}VF_3$ projected down the *a* axis. Superstructure spots indicate a tripling of the *c* axis. (The vertical direction is [010]*.)

seen in the samples of $K_{0.225}VF_3$, $Rb_{0.25}VF_3$, and $Rb_{0.225}VF_3$ (Fig. 10). Several diffraction patterns showed this superstructure clearly, but only one region was imaged. The thickness of the imaged crystal was estimated to be a few hundred angstroms. Only 7.5-Å fringes were visible, in a repeating pattern of two light fringes and one darker one. The total periodicity was thus 22.5 Å, corresponding to six *A* atom sites along *c*. The number and clarity of these diffraction patterns, together with the corresponding fringe image and the observation that they occur in a specific narrow composition range, are sufficient evidence to designate this as a separate phase, α_{IV}.

A doubling of the *a* axis could be seen only in one of the three possible [120] projections since the specimen tilt is not enough to see both [120] and [001]. This doubling was not observed on any diffraction pattern, but too few diffraction patterns were taken to conclude that the *a* axis is definitely not doubled. It is therefore uncertain whether the *c* axis image of this structure appears as α_I or α_{II}.

Elemental Analysis

A number of crystals from each of the two samples $Rb_{0.20}VF_3$ and $Rb_{0.25}VF_3$ were studied by quantitative X-ray microanalysis. Both α_I and α_{II} crystals were included. In both cases an even distribution was observed across a composition range of three to four in weight percent Rb, or about 0.04

to 0.05 in x for Rb_xVF_3. The error involved is probably great enough that a change of ± 0.03 in x would not be significant, but it is certain that, for instance, $Rb_{0.20}VF_3$ and $Rb_{0.030}VF_3$ would be distinguishable from each other in the $Rb_{0.25}VF_3$ bulk sample. Since crystals of both α_I and α_{II} were analyzed, this indicates that there is no large composition difference between them. The resolution and distribution of the data would allow a single composition or a moderate composition separation equally well.

Ionic Mobility

On several occasions it appeared that an α_{II} diffraction pattern changed to that of α_I before it could be photographed. This led to attempts to induce the transition in crystals that were more stable. The results of one partially successful attempt are shown in Fig. 11. The three figures are sequential images of a crystal from a $Rb_{0.25}VF_3$ sample. The zone axis is [111]. Figure 11a shows the α_{II} structure with alternating fringe contrast. Figures 11b and c follow at intervals of about 1 min, after heating the crystal with a bright, somewhat over-biased beam. It is clear that the thin edge of the crystal has undergone a structural change.

In Fig. 11a, the fringes are all 12.88 Å apart, indicating phase α_{II}. In Fig. 11b, after beam heating, some streaks have appeared where the 12.88-Å fringes have been replaced by a pattern of equivalent dots repeating every 6.44 Å in the direction perpendicular to the remaining fringes. These dots are characteristic of phase α_I. The streaks of phase α_I have grown into larger areas of α_I in Fig. 11c. The subcell structure appears to remain intact. The change propagates easily along a row of tunnels once it has begun, but does not extend into the thick region. This observation suggests that there can be considerable ionic mobility for the A cations at temperatures where the network of VF_6 octahedra is quite stable.

Discussion

Some general conclusions regarding the structure of α_I and α_{II} phases can be drawn from the TEM images. Phase α_I is partially ordered such that alternate (001) planes of K atom sites in the [001] direction have different occupancy factors. This may also be true for the other A atoms. Phase α_{II} also has ordering along [001], and an additional ordering of alternate (120) planes.

Several other observations must be considered in assigning the structures described above to temperature and composition ranges. For all A cations except Cs, α_I and α_{II} both exist across the entire composition range as shown by the c axis electron diffraction patterns (Table II). Also α_{II} is converted to α_I by electron beam heating in the microscope, which suggests high ionic mobility. Elemental analysis indicates that α_I and α_{II} cover the same composition range. A summary of the data suggests the diagram in Fig. 12. This drawing is introduced to make the following discussion clearer. Construction of a more complete phase diagram could be accomplished with data from high-temperature X-ray powder diffraction.

The fact that for most A cations both α_I and α_{II} appear across the entire composition range of this study might suggest a wide two-phase region, however, the X-ray elemental analysis indicates that no such region exists. Evidence that α_{II} can transform to α_I on heating places α_I at a higher temperature than α_{II}, and suggests that they can have the same composition. This is in agreement with the X-ray elemental analysis.

It is estimated that the temperature of the phase transition in the microscope was between 300 and 500°C. Since this transformation occurs rather quickly in the microscope, it seems reasonable that there was sufficient time and enough ionic mobility for a partial transition from α_I and α_{II} to


a

FIG. 11. Disordering of phase α_{II} in $Rb_{0.25}VF_3$ produced by electron beam heating. (a) Before heating. (b) after heating, (c) after further heating. The image axis is [111].

FIG. 11—*Continued.*

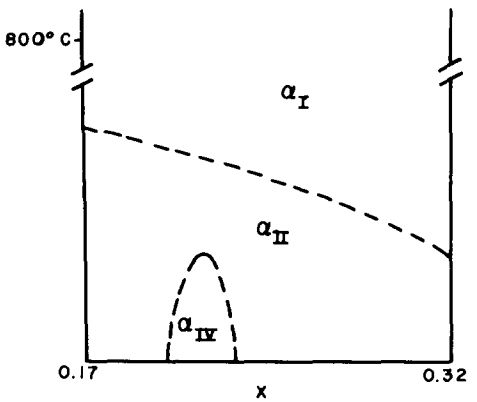

FIG. 12. Unscaled sketch of hexagonal A_xVF_3 phase relationships.

take place during the slow quench from 800°C in the synthesis. Their wide composition ranges show that α_I and α_{II} are nonstoichiometric, and so to some extent disordered.

The negative slope of the phase boundary is somewhat arbitrary, but the fact that the Cs-containing samples change to α_{II} for low x values but not for higher ones indicates that the additional ordering takes place more easily at $x = 0.18$. The ordering is more accessible at $x = 0.18$ compared to the other compositions either because the transition temperature is higher at $x = 0.18$ or because the A atom mobility is greater at a given temperature for that composition. Both of these conditions imply a downward slope. Figure 12 is a composite sketch, including features from each system.

The phase with the tripled c axis (α_{IV}) is found only near $x = 0.225$. The range of temperature over which it exists is unknown, and the representation on the sketch was chosen because it is a construction which is common in order–disorder phase diagrams. There is insufficient data to assign α_{III} a position on the sketch.

It is observed for all A cations that the site is larger than the ion. The Shannon and Prewitt radius of the 12-coordinate Cs^+ ion (1.88 Å) still leaves it about 0.1 Å from contact with the fluoride ions. Further, the fluoride ions do not touch each other around the V^{III} ions, assuming a perfect octahedron. That suggests that the energy cost of distorting an octahedron is small. All of the ions have the possibility of being off-center in the tunnel. This may account for ordering of cations to form α_{II}, even for compositions where x is nearly 0.33.

Movement from one site to another is hindered for all A cations. The K ionic radius interpenetrates the fluoride ions by about 0.2 Å on each of six ions when moving between sites in a tunnel. Rb interpenetrates the fluoride ions by 0.3 Å, Tl by 0.4 Å, and Cs by 0.5 Å. This represents a significant hindrance in the case of Cs, and is consistent with the fact that α_{II} is not observed in two of the Cs-containing samples.

Acknowledgments

This research was supported by National Science Foundation Grants DMR77-21843 and DMR79-26460 and by the Facility for High Resolution Electron Microscopy, established with support from the NSF Regional Instrumentation Facilities Program (Grant CHE-7916098). The analytical SEM was provided by funds from an NSF grant, and is currently supported by Grant ENV 76-17130.

References

1. Y. S. HONG, R. F. WILLIAMSON, AND W. O. J. BOO, *Inorg. Chem.* **18,** 2123 (1979).
2. C. CROS, R. FEURER, M. POUCHARD, AND P. HAGENMULLER, *Mater. Res. Bull.* **10,** 383 (1975).
3. A. MAGNÉLI, *Acta Chem. Scand.* **7,** 316 (1953).
4. R. LANGLEY, D. RIECK, H. EICK, L. EYRING, R. F. WILLIAMSON, AND W. O. J. BOO, *Mater. Res. Bull.* **13,** 1297–1303 (1978).
5. S. IIJIMA, *J. Appl. Phys.* **42,** 5891 (1971).
6. S. IIJIMA, *Acta Crystallogr. Sect. A* **29,** 18 (1973).
7. J. M. COWLEY AND A. F. MOODIE, *Acta Crystallogr.* **10,** 609 (1975).
8. A. J. SKARNULIS, E. SUMMERVILLE, AND L. EYRING, *J. Solid State Chem.* **23,** 5971 (1978).
9. M. A. O'KEEFE, P. R. BUSECK, AND S. IIJIMA, *Nature* **274,** (5669) 322 (1978).
10. A. RAE SMITH AND L. EYRING, *Ultramicroscopy* **8,** 65 (1982).
11. DAVID RIECK, R. LANGLEY, AND L. EYRING, to be published.